FEATURES OF THE INITIAL STAGE OF FORMATION
OF FAST CORONAL MASS EJECTION ON FEBRUARY 25, 2014

V.G. Eselevich
Institute of Solar-Terrestrial Physics SB RAS,
Irkutsk, Russia, esel@mail.iszf.irk.ru

M.V. Eselevich
Institute of Solar-Terrestrial Physics SB RAS,
Irkutsk, Russia, mesel@iszf.irk.ru

Abstract. We have analyzed the fast coronal mass ejection (CME) that occurred on February 25, 2014. The analysis is based on images taken in the 131, 211, 304, and 1700 Å UV channels of the SDO/AIA instrument and from observations obtained in the Hα line (6562.8 Å) with the telescopes of the Teide and Big Bear Observatories.

The February 25, 2014 CME is associated with the ejection and subsequent explosive expansion of the magnetic flux rope, which appeared near the solar surface presumably due to the tether-cutting magnetic reconnection.

The impulse of full pressure (thermal plus magnetic) resulting from such an "explosion" acts on the overlying coronal arcades, causing them to merge and form an accelerated moving frontal structure of the CME. This pressure impulse also generates a blast collisional shock wave ahead of the CME, whose velocity decreases rapidly with distance. At large distances $R>7R_0$ (R_0 is the solar radius) from the center of the Sun in front of the CME, a shock wave of another type is formed — a "piston" collisional shock wave whose velocity varies little with distance.

At $R \geq 15R_0$, there is a transition from a collisional to a collisionless shock wave.

Keywords: coronal mass ejection, magnetic rope, coronal arcades, blast shock wave, solar wind, collisional and collisionless shock waves.

INTRODUCTION

From the results of experimental studies and the use of modeling techniques, it has been reliably established that a typical coronal mass ejection (CME) is a magnetic flux tube filled with plasma whose two bases are rooted in the photosphere [Krall et al., 2000; Thernisien et al., 2009]. Note that the magnetic flux tube as a twisted magnetic tube has an additional magnetic field component perpendicular to the main longitudinal field of the tube. In theory for the sake of simplicity, the magnetic flux tube is generally considered.

According to kinematic characteristics, CMEs are divided into two groups: gradual (slow evolving) and impulsive [Sheeley et al., 1999]. CMEs, although by other names (flare-associated and eruption-associated), were first classified in [MacQueen, Fisher, 1983].

The CME formation mechanism is still unclear. Especially unclear is one of the main moments of CME formation, namely, whether the magnetic tube (rope) in all cases exists and is located above the photosphere (in the chromosphere/corona) before the eruption or it, at least in some events, may be erupted from the convection zone. The answer to this question determines, to some extent, the validity of the classification of CMEs into gradual and impulsive, and hence the possibility of existence of at least two different CME formation mechanisms.

The existence of gradual CMEs has been proved experimentally. In particular, Patsourakos et al. [2013] were the first to observe and study the evolution of the magnetic rope of a gradual CME (July 19, 2012) on the limb, which formed over an active region at a very low height $h<0.2R_0$ (R_0 is the solar radius). A number of papers [Hundhausen, 1999; Sheeley et al. ,1999; Bemporad et al., 2007; Eselevich, Eselevich, 2011] describe the formation of gradual CMEs at $0.1R_0<h<1.0\ R_0$.

Picture of the formation of gradual CMEs is as follows. In the corona there is a magnetic rope filled with plasma whose two bases are rooted in the photosphere. In response to the development of instability, it erupts from the Sun. The instability type that leads to the eruption and causes of its development are not entirely clear, despite a number of mechanisms being examined [Antiochos et al.,1999; Amari et al., 2000; Magara, Longcope, 2001; Gibson et al., 2006; Archontis, Hood, 2008].

As one of the most common mechanisms of magnetic rope formation and its subsequent eruption a so-called tether-cutting magnetic reconnection is considered [Moore, LaBonte, 1980; Moore et al., 2001]. During this process, the system of crossed magnetic loops with shear reconnect above the neutral magnetic line, thus leading to the formation of the rope and its subsequent eruption due to reduction in the dampening effect of magnetic tension. The validity of the tether-cutting model is confirmed by a number of observations and numerical calculations (e.g., [Zhang et al., 2001; Sterling, Moore, 2005]). The possibility of contribution of the kink instability to the eruption is also discussed [Kliem et al., 2004; Shen et al., 2012].

According to [Schmieder et al., 2013], more than 80 % of all observed CMEs are triggered by eruption of solar filaments, which in fact are also magnetic ropes or are located inside the ropes. A possible way of implementing this trigger mechanism is described in [Grechnev et al., 2016; Fainshtein, Egorov, 2015].

Another CME type is impulsive CMEs. Their formation is assumed to be linked to the eruption of a magnetic flux tube with a relatively cold plasma from

the convection zone. This possibility has been predicted within the theory of thin magnetic flux tube as a result of the development of a slow wave or Parker instability [Moreno-Insertis et al., 1992; Alekseenko et al., 2000; Romanov et al., 1993a]. The main conclusions of the theory and their comparison with experimental results are given in [Romanov et al., 1993b; Eselevich et al., 2013; Eselevich, Eselevich, 2014].

To directly prove the eruption of magnetic flux tubes from the convection zone, which trigger CMEs of this type, it is desirable to have solar magnetic field measurements with a time resolution ~1–10 s, which cannot be provided by modern magnetographs, such as SDO/HMI and SOHO/MDI having a resolution of ~1 min.

Nonetheless, a quickly emerging magnetic flux tube can be detected by indirect methods. Eselevich, Eselevich [2015] through the analysis of the January 5, 2013 event without eruption of matter (active prominence, or jet) have shown the following: CME might be formed by ejection of a plasma portion (cavity) with lower brightness from the Sun, as viewed in the 193 Å channel. After analyzing the three-dimensional structure of the cavity, its dynamics and kinematics, and comparing the analysis results with theoretical predictions, the authors could identify the cavity with the magnetic flux tube (rope) filled with cold and rarefied (compared to ambient) plasma ejected at high speed from the convection zone to the solar atmosphere.

A similar situation was recorded for the CMEs that occurred on April 27, 2011 [Eselevich, Eselevich, 2013] and on March 25, 2008 [Eselevich, Eselevich, 2011], which were accompanied by an active prominence (jet).

There is also a point of view that impulsive CMEs may arise from imbalance in existing magnetic ropes (see, e.g., [Temmer et al., 2008; Zagainova, Fainshtein, 2015; Eselevich et al., 2016]).

The aim of this work is to study features of the formation of the February 25, 2014 CME and its related shock wave. The initial phase of this event has already been investigated in [Chen et al., 2014] and it has been found that the eruptive magnetic rope is formed due to tether-cutting reconnection.

1. DATA AND METHODS OF ANALYSIS

Analysis is based on UV images taken with SDO/AIA in the 131, 171, 211, 304, 1700 Å channels [Lemen et al., 2012]. The time interval between the SDO/AIA images is ~12 s, spatial resolution is 1.2 arcsec (two pixels), which corresponds to $0.00125R_0$, if expressed in fractions of the solar radius. The field of view of the instrument is up to ~1.4 R_0.

We have also used images obtained in the Hα line (6562.8 Å) with telescopes of the Teide (Spain) and Big Bear (USA) observatories under the NSO Synoptic Integrated Program (NISP) [https://www.nso.edu/telescopes/nisp] with a time resolution of ~1 min.

White-light corona, Hα, and UV images were presented as difference brightness images with a fixed initial time

$$\Delta P = P(t) - P(t_0),$$

where $P(t_0)$ is the undisturbed brightness at t_0 before the event of interest; $P(t)$ is the disturbed brightness at any $t>t_0$.

We have used the difference images (Figure 1) to study the CME dynamics. To do this, we plotted distributions of $\Delta P(R)$ relative to the solar center along the radius at a fixed position angle PA at different times. The position angle PA is measured in solar images from the north pole counterclockwise. In some cases, we utilized running difference brightness images $\Delta P_R = P(t_i) - P(t_{i-1})$, i.e. constructed from two images adjacent in time.
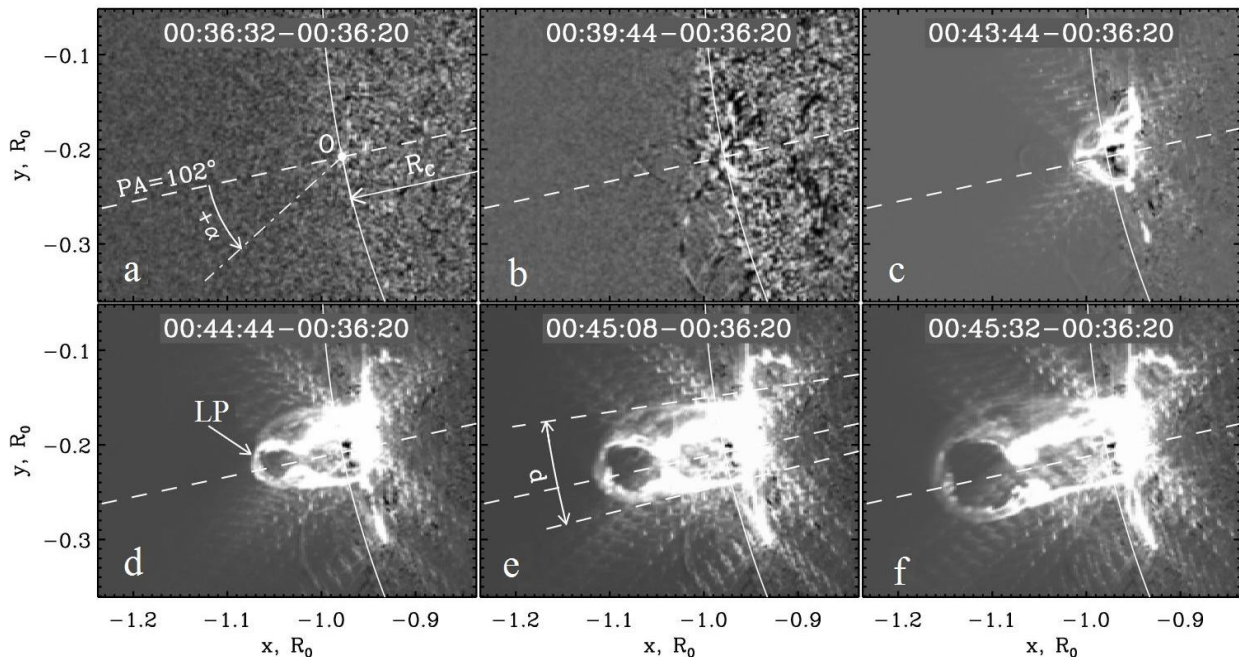

Figure 1. Difference images in the 304 Å channel for successive points in time showing the evolution of the February 25, 2014 CME (from SDO/AIA data). Positive counting of the distance from the center of the Sun along the Y-axis — to the north, along the X-axis — to the west. Distances are normalized to the solar radius R_0

The difference brightness images were used to construct the distributions of $\Delta P(r)$ or $\Delta P_R(r)$ at different angles α relative to the axis of CME motion (directed along a certain PA) with an averaging angle $\delta\alpha$ at different times (the α angle estimate is positive counterclockwise, Figure 1, *a*). Distance r was measured from the center O, located along the axis of CME motion at R_c from the Sun's center (in Figure 1, *a*, $R_c=1R_0$). The distances R from the Sun's center and r are related by $R=(R_c^2+r^2+2rR_c\cos\alpha)^{1/2}$.

2. ANALYSIS OF THE FEBRUARY 25, 2014 CME

2.1. Dynamics of CME occurrence according to data in cold UV channels (304 Å, 1700 Å) and in the Hα line

The event of interest occurred in active region 11990 (heliographic coordinates S15, >E65) and was accompanied by an X4.9 flare at 00:39 UT on February 25, 2014. Coordinates of the flare are S12E82, i.e. the event took place on the visible portion of the disk near the limb.

Pictures of the initial phase of the CME differ when observed in relatively cold channels of 1700 Å ($T\approx5\cdot10^3$ K), 304 Å ($T\approx5\cdot10^4$ K), Hα line 6562.8 Å ($T\approx8\cdot10^3$ K), and in hot channels of 131 Å ($T=10^7$ K), 171 Å ($T=6.3\cdot10^5$ K), and 211 Å ($T=2.1\cdot10^6$ K) [Lemen et al., 2012]. Thus, for the 171, 193, and 211 Å channels, the temperatures correspond to the temperature response function maximum; and for the 131 Å channel, the temperature corresponds to the hottest local maximum of temperature response function.

It is important to note that the 1700 Å channel reflects the band in the vicinity of the respective wavelength of the continuous spectrum of solar surface emission in a blackbody approximation [Vernazza et al., 1973; Gibson, 1977]. Within this approximation, it allows us to estimate the minimum photospheric temperature (region of minimum temperature) at heights 400–600 km [Vernazza et al., 1976].

Let us study the initial phase of this CME by considering running difference brightness images in the cold channel of 304 Å at successive points in time (Figure 1, *a–f*). It is clear that before the event at $t_0\approx00:36:32$ UT in difference images there are no disturbances (Figure 1, *a*). This, however, is not entirely consistent with AIA/SDO direct images. Chen et al. [2014] have analyzed a sequence of AIA/SDO direct images in the 94, 131, 211, 304 Å channels for the February 25, 2014 CME and have shown that there was a filament (prominence) in the active region before the eruption and the flare, as well as a system of magnetic loops crossed over the neutral line. This is well illustrated in Figure 2 [Chen et al., 2014], in which the filament is seen until 00:35 UT.

The authors [Chen et al., 2014] argue convincingly in favor of the formation of the magnetic rope containing the filament through the tether-cutting magnetic reconnection.

The system of crossed magnetic loops with shear reconnects over the neutral magnetic line, thus leading to the formation of a rope containing a filament and their subsequent eruption due to a decrease in magnetic tension. Since the velocity of the filament is close to the velocity of the rope, the kinetic energy of the filament, in view of the higher density of material in it, is obviously much greater than the kinetic energy of the rope. Therefore, the role of a moving filament in disturbing the ambient corona is crucial. This paper also discusses the possibility of kink instability contribution to the eruption.

Let us analyze the dynamics of the event for $t_0\approx00:36:32$ UT on the basis of the temporal sequence of difference brightness images presented in Figure 1. From ~00:39:32 UT (this point in time is absent in Figure 1) near the limb at $R\approx1.0\ R_0$ (at ~ 00:39:44 UT, Figure 1, *b*), a small arcade with increasing brightness appears. The arcade (its leading part is designated as LP in Figure 1, *d*) first is left in place and then begins gradually moving from the Sun to the position angle $PA\approx102°$ (dashed line in Figure 1). Subsequent images (Figure 1, *e – f*) show rapid acceleration and expansion of this bright arcade, which takes the form of a shell encompassing a dark cavity (its angular size d is displayed in Figure 1, *e*) — it is, in fact, a characteristic
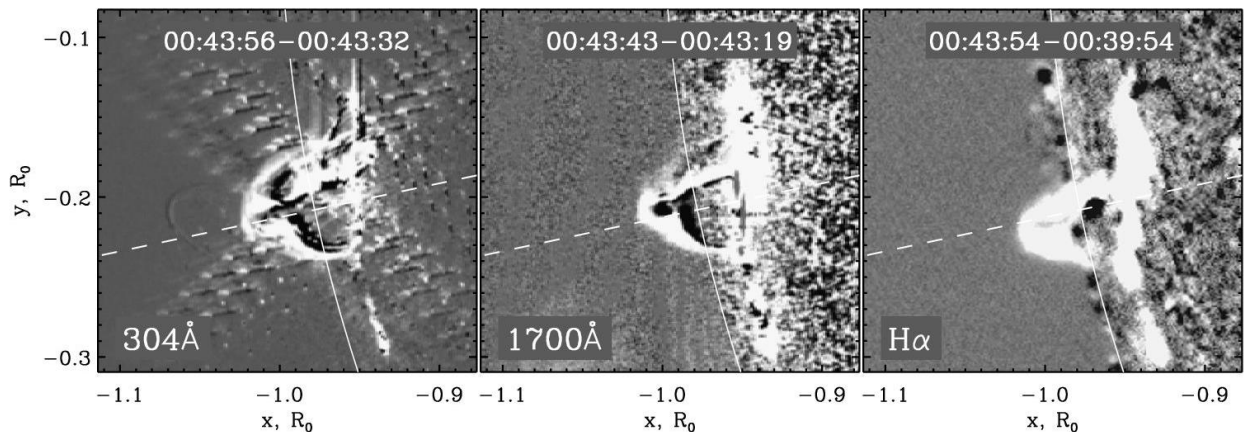

Figure 2. Difference images obtained for close times in the 304 and 1700 Å channels and in the Hα line (according to data from SDO/AIA and telescopes of the Teide (Spain) and Big Bear (USA) observatories under NISP [http://gong2.nso.edu])

cross-section of the magnetic flux tube (rope) with plasma, which is usually called active prominence [Priest, 1985]. The magnetic rope in the cold channel of 1700 Å and in the Hα line exhibits a similar development. This is evident from the comparison between difference images for close moments in both cold (Figure 2) and hot channels (see, e.g., Figure 3). However, in hot channels such as the 211 Å channel, in addition to the heated shell of the erupted magnetic rope we can watch other CME formation signatures in the corona, which are recorded as arcades (marked with numerals 1, 2, 3 in Figure 3, *a*, *b*). This will be discussed in more detail in what follows.

The formation of the erupted magnetic rope, or rather its leading part (LP), can be analyzed in greater detail from difference brightness distributions $\Delta P(R)$ in the 304 Å channel, built in the direction of $PA \approx 102°$ (dashed line in Figure 1) at $t_0 = 00:36:20$ UT (averaged over the angle $\delta\alpha = 1°$) for successive points in time on February 25, 2014 (Figure 4).

Figure 4, *a*, *b* shows that from $t \geq 00:36:32$ UT, LP of the magnetic rope is formed: the maximum of its difference brightness ΔP_{max} increases, while remaining at $R \approx 1.003\ R_0$ nearly until $t \approx 00:42:08$ UT (Figure 4, *a*, *b*). This means that, when formed, the magnetic rope was near the solar surface and its brightness began enhancing due to the development of some dissipative processes in it.

The spatial size δ_l of the decrease in ΔP_{max} to $\Delta P_{max}/10$

is shown in Figure 4, *b–h* by a horizontal dashed line. According to [Eselevich, 2010], it characterizes the width of the current sheet of a spatial plasma density irregularity with frozen magnetic field or the width δ_l of the magnetic rope LP front in the ΔP profile. The possibility of such identification of δ_l is due to the fact that to an abrupt change in ΔP_{max} on a sufficiently small spatial scale should correspond a plasma density irregularity in the corona. In turn, the rarefied plasma density irregularity can be provided only by the magnetic field irregularity (due to its freezing in plasma), which is equivalent to the presence of current on the same scale (for more detail, see [Eselevich, 2010]).

The δ_l value remains virtually constant until $t \geq 00:43:56$ UT (Figure 4, *d*), then δ_l begins increasing rapidly as the difference brightness maximum of the magnetic rope LP moves away from the Sun (Figure 4, *e–h*). We can try to understand the reason by analyzing Figure 5, which shows a number of dependences in the direction of the position angle $PA = 102°$ (at $R_c = 0.97\ R_0$; $\delta\alpha = 1°$) for the magnetic rope LP.

A kinematic curve of $R/R_0(t)$ for the middle point of the magnetic rope LP (cross in Figure 4) is presented in Figure 5, *a*. It was used to plot the dependence of $V(R)$ in Figure 5, *c* from the formula $V = (R_{i+1} - R_i)/(t_{i+1} - t_i)$.
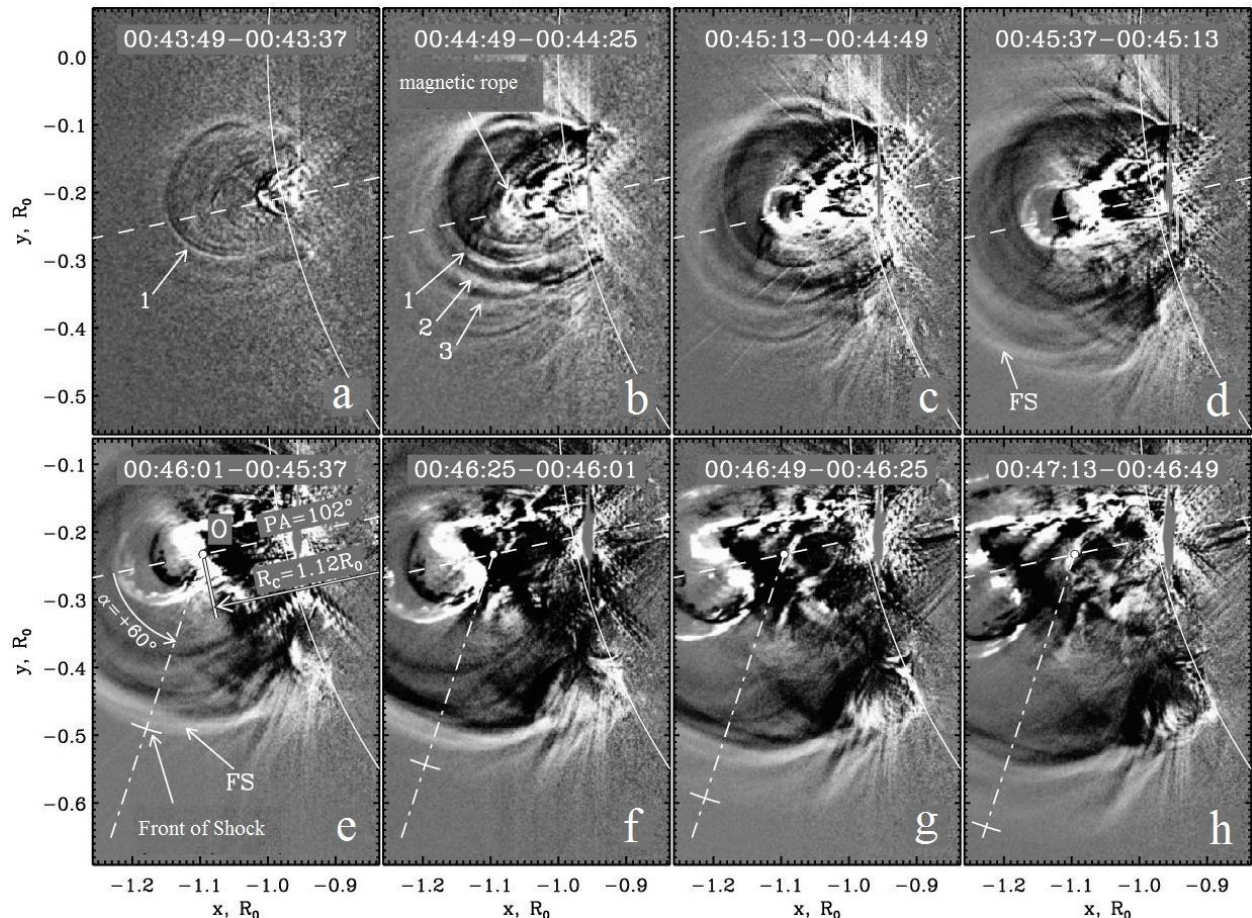

Figure 3. Running difference brightness images in the 211 Å channel for successive points in time showing the development of the February 25, 2014 CME (SDO/AIA data). FS is the CME frontal structure
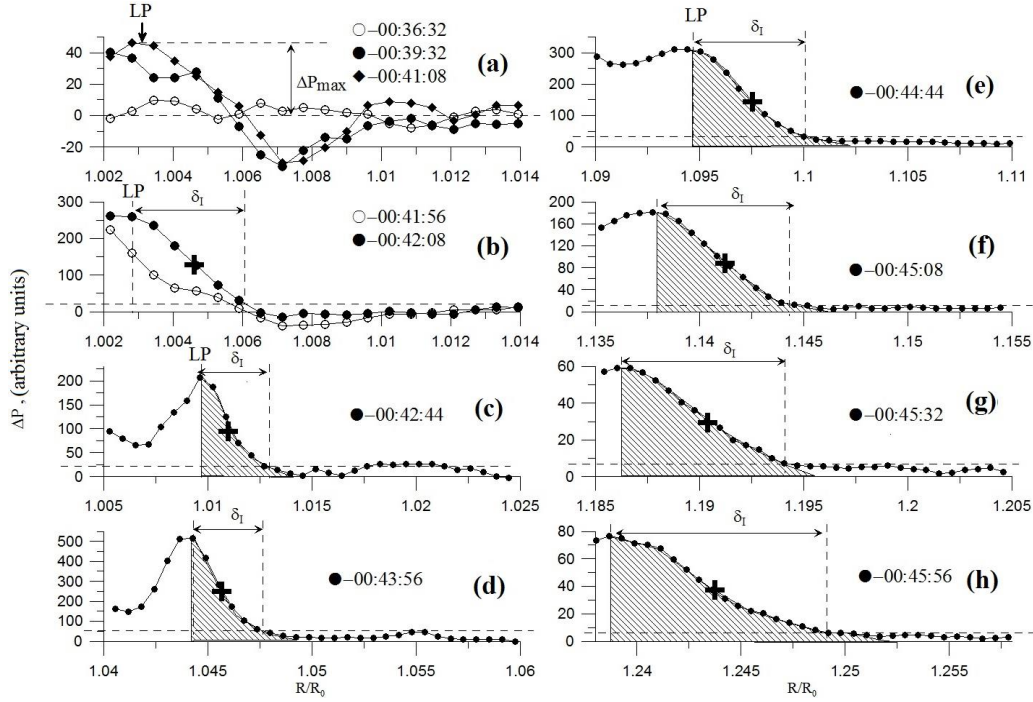
Figure 4. Difference brightness distributions ΔP as a function of distance R in the direction of the position angle $PA=102°$ (at $t_0=00:36:20$; $R_c=0.97\ R_0$; $\alpha=0°$; $\delta\alpha=1°$) at successive points in time for the leading part (LP) of the magnetic rope in the February 25, 2014 event (according to AIA/SDO data in the 304 Å channel). The cross marks the middle point of the magnetic rope LP
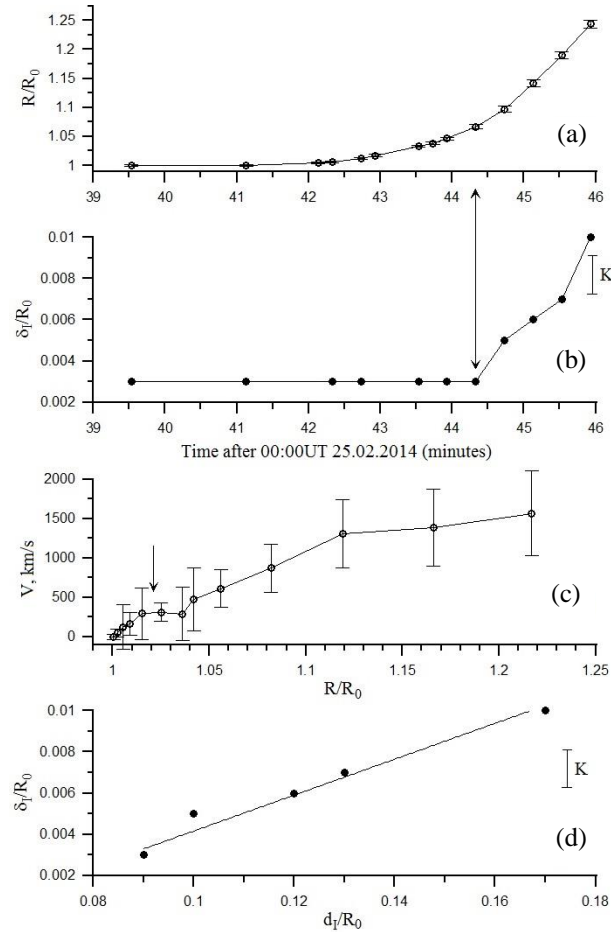

Figure 5. Dependences in the direction of the position angle $PA=102°$ (at $R_c=0.97\ R_0$; $\alpha=0°$; $\delta\alpha=1°$) for the leading part of the magnetic rope in the February 25, 2014 event

Here, in the numerator is the difference between adjacent points along the X-axis in Figure 5, *a*; in the denominator is the time interval between them. Referring to Figure 5, *a*, after the gradual increase in the velocity from zero the second notable acceleration of LP occurs at $t\geq00:44:00$ UT (Figure 5, *a*) at a distance $R\geq1.025\ R_0$ (on the $V(R)$ plot (Figure 5, *c*), the onset of the second acceleration is indicated by a vertical arrow). This acceleration is connected with the onset of the sharp increase in the width δ_I of the magnetic rope LP front in Figure 5, *b* (vertical arrow). As can be seen from Figure 5, *d*, at $t\geq00:44:00$ UT at $R\geq1.025\ R_0$ a rapid expansion of the magnetic rope in transverse direction and, correspondingly, an increase in its angular size d_I also begin. Here, δ_I increases almost linearly as a function of d_I (Figure 5, *d*). It is conceivable that one of the likely reasons for the increase in δ_I with time at this stage is that the estimated difference brightness ΔP is averaged over the length of the structure along the line of sight, increasing due to increasing magnetic rope diameter d_I.

2.2. Estimated plasma temperature distribution in LP of the erupted magnetic rope

To estimate the plasma temperature distribution in LP of the erupted magnetic rope, we analyze the spatial difference brightness distributions normalized to ΔP_{max} in LP in the direction of $PA=102°$ for several different UV channels and in the Hα line.

First, let us compare the distributions $\Delta P(R)/\Delta P_{max}$ in the 1700 Å cold channel ($T\approx5\cdot10^3$ K) and in the Hα line ($T\approx8\cdot10^3$ K) and in the hot channels of 171 Å ($T=6.3\cdot10^5$ K) and 211 Å ($T=2.1\cdot10^6$ K) at an early stage of the event development at $t\approx00:42:55$, when the magnetic flux tube

began moving with a relatively low velocity of ~60 km/s. With such a velocity of the magnetic flux tube and ≤6 s difference in the time of recording between different channels and the Hα line, a shift between their profiles is negligible: ≤0.0005 R_0. Figure 6, *a* suggests that positions of profile maxima in the 1700 Å channel (open circles) and in the Hα line (black triangles) roughly coincide. The profile width in the Hα line is ~1.5 times larger than that in the 1700 Å channel. Distribution profiles in the hot channels of 171 Å (open triangles) and 211 Å (crosses) are much narrower than those in cold channels. Distribution maxima $\Delta P(R)/\Delta P_{max}$ in hot channels coincide in position and are located more to the left than those in the 1700 Å channel and in the Hα line.

Figure 6, *b* compares the spatial distributions $\Delta P(R)/\Delta P_{max}$ in cold (304, 1700 Å) and hot (131, 211 Å) channels for a later time when the magnetic flux tube was located in the corona and had a velocity of over 1000 km/s. When constructing the plot, we take as a basis the position of the distribution maximum $\Delta P(R)/\Delta P_{max}$ for the 304 Å channel at 00:44:44 UT, whose difference brightness profile has been shown in Figure 4, *e*.

By this time, the $\Delta P(R)$ profiles in all the channels are fairly clearly recorded (except for Hα) and their maxima move with a velocity $V \approx 100$ km/s in the radial direction at distances $R \approx (1.08 \div 1.12) R_0$ (Figure 5, *c*).

Moments of recording for different channels differ by $\Delta t \le 11$ s. Given the propagation velocity $V \approx 1100$ km/s at the selected distance, the difference in Δt for profiles in different channels is compensated by their respective shift in space by $-\Delta R \approx (-\Delta t) V$ (i.e., to the negative side with respect to the position of the profile in the 304 Å channel). Thus, for the 304 Å channel at t=00:44:44 UT ΔR=0, for the 1700 Å channel at t=00:44:55 UT ΔR=–0.0176 R_0, for the 211 Å channel at t=00:44:49 UT ΔR=–0.008 R_0, for the 131 Å channel at t=00:44:46 UT ΔR=–0.003 R_0.

Referring to Figure 6, *b*, in the general case brightness profiles of the magnetic rope LP in the hot channels of 131 Å (black diamonds), 211 Å (crosses), as well as in the cooler channel of 304 Å (black circles) have already two adjacent maxima (at $R \approx 1.087 R_0$ and $R \approx 1.094 R_0$).

First, compare the distributions $\Delta P(R)/\Delta P_{max}$ in the 1700 Å cold channel and in the Hα line with the distributions in the hot channels of 171 Å and 211 Å at the early stage of the event development at $t \approx 00:42:55$ UT.

The interior maximum at $R \approx 1.087 R_0$ (Figure 6, *b*), in contrast to the previous time (Figure 6, *a*), is linked to the profile in the 1700 Å channel (line with open circles, gray background). Before it at $R \approx 1.094 R_0$ (Figure 6, *b*), narrow peaks appear in the profiles in the channels of 211 Å (crosses, marked with horizontal hatching) and 131 Å (diamonds) corresponding to temperatures of $2.1 \cdot 10^6$ and $2 \cdot 10^7$ K [Lemen et al., 2012].

On further motion of CME at t=00:44:55 (Figure 6, *c*), the difference brightness profile of LP in the 211 Å hot channel (crosses) already has one maximum, still shifted to the right with respect to the profile maximum in the 1700 Å cold channel (open circles). In Figure 6, *c*, for the profile in the 1700 Å channel ΔR=0, while in the 211 Å the channel ΔR=–0.003 R_0 with $V \approx 1160$ km/s.
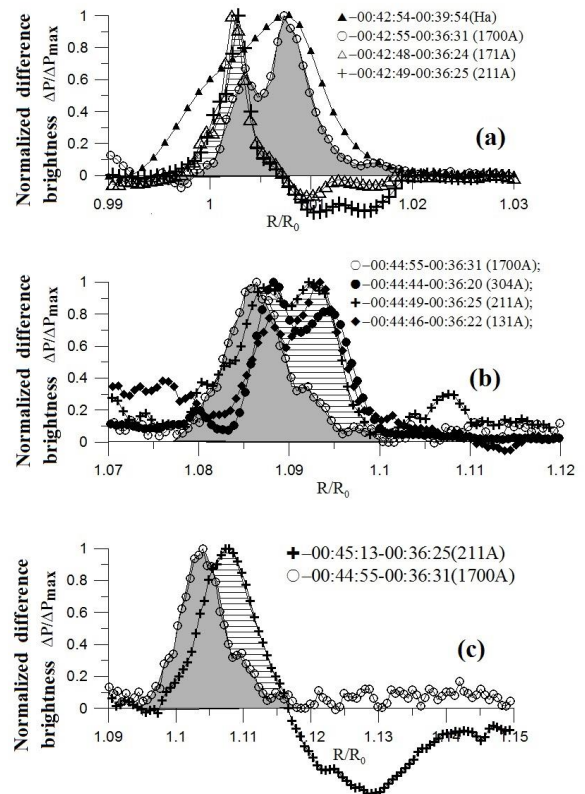

Figure 6. Spatial difference brightness distributions $\Delta P(R)$ normalized to ΔP_{max} in the direction of PA=102° ($\delta\alpha$=1°) in UV channels and in the Hα line for three consecutive times: *a* — at a time close to $t \approx 00:43:00$ UT in the Hα line (black triangles, $t \approx 00:42:54$ UT) and in the channels of 1700 Å (open circles, $t \approx 00:42:55$ UT), 171 Å (open triangles, $t \approx 00:42:48$ UT), 211 Å (crosses, $t \approx 00:42:49$ UT); *b* — $\Delta P(R)$ at t=00:44:55 UT normalized to this time by shifting to a distance ΔR with a velocity of the structure $V \approx 1100$ km/s, in the channels of 131 Å (black diamonds), the time of recording t=00:44:46 UT, $\Delta R \approx$ –0.003 R_0; 211 Å (crosses), t=00:44:49 UT, $\Delta R \approx$ –0.008 R_0; 1700 Å (open circles), t=00:44:55 UT, $\Delta R \approx$ –0.0176 R_0; *c* — at $t \approx 00:44:55$ UT in the 1700 Å and 211 Å channels. The profile in the 211 Å channel was recorded at t=00:44:49 UT and normalized to t=00:44:55 UT by shifting to $\Delta R \approx$ –0.003R_0 at $V \approx 1160$ km/s. The February 25, 2014 event, SDO/AIA and NISP data [http://gong2.nso.edu]

This pattern can be interpreted in accordance with the paper by Chen et al. [2014], in which the authors, by analyzing AIA/SDO direct images, have shown that in this event a part of the cold filament (the outer shell whose brightness profiles in the 1700 Å channel and in the Hα line are presented in Figure 6, *a*) at the beginning of the event was located over a part of the magnetic loops making up the magnetic rope (the inner shell; brightness profiles in the 131 and 211 Å channels in Figure 6, *a*). After the tether-cutting reconnection, at least a part of field lines of the eruptive rope, visible in the 131 Å hot channel, rose above the cold material of the filament (the outer shell; brightness profiles in the 131 and 211 Å channels in Figure 6, *b*).

Moreover, this process can be enhanced as the CME is moving away from the Sun: as shown in Figure 5, *b*, after $t \approx 00:44:00$ UT an explosive expansion of the magnetic flux tube begins in all directions. As a result, the temperature distribution inside LP can change rapidly:

the outer shell becomes hotter, $T \geq 2 \cdot 10^6$ K than the inner shell with $T \approx 5000$–8000 K (Figure 6, *b*, *c*). More accurate temperature values in the shells can be provided by a more detailed quantitative analysis of brightness in different channels.

2.3. Dynamics of CME occurrence in the 211 Å hot channel

In the hot channels of 94, 171, 193, and 211 Å, besides the heated shell of the erupted magnetic rope with a relatively cold plasma, we can watch other signatures of CME formation in the corona. This is a fundamental difference between difference brightness images in hot channels and images in cold channels. Let us examine this difference by the example of images in the 211 Å channel.

Compare the difference brightness images for adjacent points in time, which are displayed in Figure 2 and Figure 3, *a*. The images in the 304, 1700 Å cold channels and in the Hα line (Figure 2) demonstrate only the erupted magnetic rope the dynamics of the leading part of which has been analyzed above. The running difference brightness images in the 211 Å hot channel (Figure 3, *a*) besides the magnetic rope exhibit an arcade, marked with numeral 1. At subsequent times in the 211 Å channel, arcades 2 and 3 become visible (Figure 3 *b*, *c*). The shape of the arcades is close to circle. Dynamics of these arcades for three consecutive times reflecting the initial phase of the evolution of the event is seen in the images from the 211 Å channel (Figure 3, *a–e*). Over time, expanding, they move away from the Sun and merge into one frontal structure (FS) of CME (Figure 3, *d*, *e*).

Because of the limited field of view on the left, let us analyze spatial distributions of the running difference brightness $\Delta P_R(r)$ in the direction of the angle $\alpha=60°$ (dash-dot line in Figure 3, *e–h*) originating from the center O, located at a distance $R_c=1.12 R_0$ along the position angle $PA=102°$ (dashed line in Figure 3) at $\delta\alpha=1°$. The analysis shows that rates of expansion of the arcades with respect to the center O are approximately equal in the directions $\alpha=0°$, $\pm60°$. The profiles of $\Delta P_R(r)$ in the direction of $\alpha=60°$ for five consecutive times are shown in Figure 7.

It can be seen that the appearance and brightness enhancement of arcade 1 occur at $t \leq 00$:43:37 UT (open and black circles in Figure 7, *a*); and those of arcades 2 and 3, at $t \geq 00$:43:37 UT (Figure 7, *b*). At $t \leq 00$:45:13 UT, arcades 4, 5, 6 of a larger diameter become visible (Figure 7, *d*). It is fair to assume that all these arcades gradually become visible due to a slight shift associated with the solar rotation. Let us explain why.

The arcades studied are recorded only in hot channels (94–211 Å) and are a cross-section of quasi-stationary coronal magnetic ropes, which contain a plasma with temperature $T \geq 2 \cdot 10^6$ K isolated by the magnetic field from coronal plasma. This means that due to the shift caused by the solar rotation, they may become visible because fall into the background of ambient plasma of the corona with a somewhat lower density.
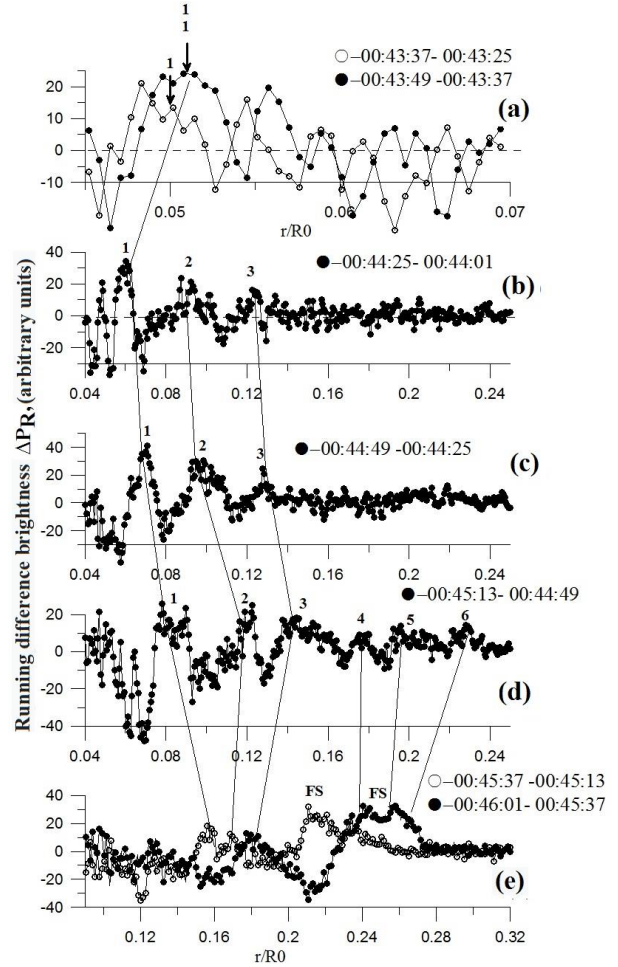

Figure 7. Running difference brightness distributions ΔP_R as a function of distance *r* in the direction of the angle $\alpha=60°$ emanating from the center O at a distance $R_c=1.12R_0$ in the direction of $PA=102°$ (see Figure 3, *e*) at $\delta\alpha=1°$ at consecutive times for arcades 1, 2, 3 (see Figure 3, *b*) and 4, 5, 6 in the February 25, 2014 event (according AIA/SDO data in the 211 Å channel)

Between $t \approx 00$:45:13 UT (Figure 7, *d*) and $t \approx 00$:45:37 UT (Figure 7, *e*, open circles), the situation changes dramatically. Arcades 1, 2, and 3 approach, catching up each other, and arcades 4, 5, 6 explosively merge into a single frontal structure (FS in Figure 7, e) of future CME, as we have noted when analyzing images in Figure 3.

The onset of these processes roughly coincides with the onset (after $t \approx 00$:44:30 UT) of the explosive acceleration and expansion in Figure 5, *a*, *b* (arrow) of the erupted magnetic flux tube with hot plasma.

Further FS dynamics in time can be observed from the running difference brightness profiles $\Delta P_R(r)$ in the direction of $\alpha=60°$ shown in Figure 8, *a–d* and duplicated in a larger scale in Figure 8, *e–h*.

In Figure 8, *e–h*, open circles indicate the $\Delta P_R(r)$ profiles for $t=00$:43:37 UT, i.e. before FS occurs at these distances *r*. The observed variations of $\Delta P_R(r)$ (open circles) characterize the noise level of the undisturbed ambient plasma and allow us to more reliably identify a region corresponding to the shock front formed before FS from 00:46:01 UT (Figure 8, *a*, *e*). The region in the distribution is marked with dark gray background, and its decreasing
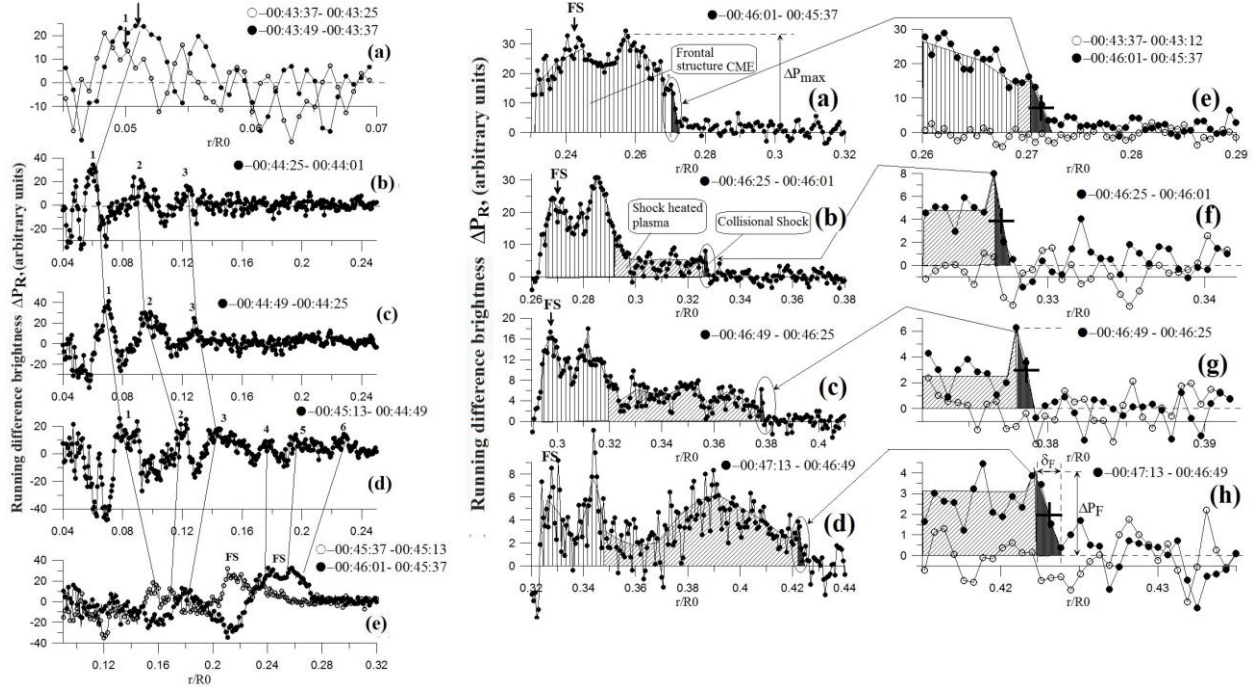
Figure 8. Running difference brightness distributions ΔP_R as a function of distance r in the direction of the angle $\alpha=60°$ emanating from the center O, located at a distance $R_c=1.12R_0$ in the direction of $PA=102°$ at $\delta\alpha=1°$, at successive points in time for the CME frontal structure (FS) (*a–d*). The same on a larger spatial scale (*e–h*). The February 25, 2014 event (according to AIA/SDO data in the 211 Å channel)

brightness profile is approximated by an inclined line. After it, the oblique hatching indicates a region of shock-heated plasma; and the vertical hatching, the CME frontal structure. The front width δ_F is defined as twice the width at half-maximum of brightness jump ΔP_F at the wave front (Figure 8, *h*). Positions of the shock front for the times corresponding to ΔP_R in Figure 8, *b–d* are marked with crosses in the running difference brightness images (Figure 3, *e–h*). Jumps of $\Delta P_R(r)$ at the shock front are low and therefore difficult to see in the difference brightness images, but they can be fairly reliably recorded from scans in the selected direction with a small averaging over the angle $\delta\alpha=1°$ (Figure 8, *a–d*). The right boundary of FS is defined in terms of the distance R at which the maximum difference brightness ΔP_{max} FS (Figure 8, *a*) is halved. Figure 8, *a–d* shows that with time the distance between the shock front and FS increases since the front velocity exceeds the FS velocity.

To understand the type of the observed front, make a comparison with the results received in [Eselevich, Eselevich, 2012]. To do this, using data presented in Figure 8, plot velocities of the frontal structure V_r^{FS} (FS in Figure 8, *a–d*) and of the shock front V_r^{Sh} (a cross in Figure 8, *e–h*) in the direction of $\alpha=60°$. Find these velocities from the formula $V(\alpha=60°, r)=(r_{i+1}-r_i)/(t_{i+1}-t_i)$, used above. Here, in the numerator is the difference in position of estimated structures between adjacent times; in the denominator, the time interval between them. For the transition from r to R, use the relation $R(r, \alpha)=(R_c^2+r^2+2rR_c\cos\alpha)^{1/2}$. Results of the plotting of $R(t)$ for FS (black circles) and shock front

(open circles) are presented in Figure 9, *a*; the relationships $V_r^{FS}(\alpha=60°, R)$ (black circles) and $V_r^{Sh}(\alpha=60°, R)$ (open circles) calculated from these curves, in Figure 9, *b*.

According to [Eselevich, Eselevich, 2012], a shock front is formed when the condition $u(R)=V_r^{FS}(R)-V_{SW}(R)>V_a$ holds, where $V_{SW}(R)$ is the velocity of the
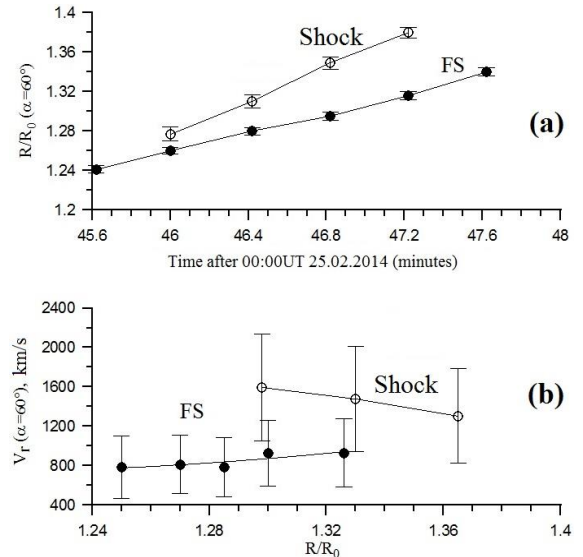

Figure 9. Kinematic dependence $R(t)$ for frontal structure (FS, black circles) and shock front (open circles) in the direction of the angle $\delta\alpha=60°$ emanating from the center O, located at a distance $R_c=1.12R_0$ in the direction of $PA=102°$ at $\delta\alpha=1°$; $R(r, \alpha)=(R_c^2+r^2+2rR_c\cos\alpha)^{1/2}$ (*a*). The FS velocity $V_r^{FS}(\alpha=60°, R)$ (black circles) and the shock front velocity $V_r^{Sh}(\alpha=60°, R)$ (open circles), calculated from the curves in Figure 9, *a*, as a function of distance R (*b*)

ambient slow quasistationary solar wind, V_a is the local Alfvén velocity. In our case, at $R \approx 1.27 R_0$, where the first occurrence of the shock front was detected, $V_a \approx 400$–500 km/s, while $V_{SW} < 10$ km/s (see Figure 5, *a* in [Eselevich, Eselevich, 2012]). According to Figure 9, *b*, $V_r^{FS}(R)$–$V_{SW}(R) \approx 800$ km/s$>V_a$, i.e. the condition for shock front excitation holds.

The front width δ_F characterizes the type of shock front or the mechanism of energy dissipation in it. Along a subpath of $\Sigma \approx (1.27 \div 1.35)R_0$, $\delta_F(R) \approx 0.0012R_0 \approx$ $\approx const$. In fact, δ_F is determined by the spatial resolution of AIA/SDO that is $K \leq 0.0017R_0$. This means that the true value of δ_F can be much smaller than that measured. At $R > 1.35R_0$, δ_F starts increasing. This behavior is consistent with Figure 5, *b* from [Eselevich, Eselevich, 2012] and is explained by the fact that at these distances R the front width δ_F is of the order of the mean free path of protons λ_p in the corona at proton-proton collisions, which increases rapidly with distance from the Sun, and at $R > 1.35R_0$ $\delta_F \approx \lambda_p$ exceeds the resolution of the instrument K. This also implies that the mechanism of energy dissipation in the shock front is collisional.

From Figure 9, *b* follow another two important features of the event under study:

1) the shock wave velocity at the time of the first recording at $R \approx 1.29R_0$ is almost twice the FS velocity;

2) the shock front velocity decreases with distance (open circles), while the FS velocity increases (black circles).

This suggests that the cause of the shock wave occurrence cannot be the magnetic piston of the CME frontal structure, i.e. the observed shock wave cannot be piston. It has all characteristics of a blast shock wave.

The above analysis allows us to conclude that the occurrence of the blast shock wave during the CME formation is linked to the explosive expansion of the magnetic flux tube with heated plasma ejected from the solar surface after $t \approx 00{:}44{:}25$ UT (see Figure 5, *b*). The resulting full pressure (thermal plus magnetic) impulse, rapidly spreading in a wide range of angles α relative to the direction of the magnetic rope motion, exerts a force on arcades 4, 5, 6 (see Figure 7, *d*, *e*), leading to their merging and to the formation of a rapidly moving CME FS. This very pressure impulse is responsible for the blast collisional shock wave before the CME FS. A similar process of shock wave excitation in the corona was called impulsive-piston excitation in [Grechnev et al., 2018].

2.4. CME dynamics at distances $6R_0 < R < 30R_0$ according to LASCO C3 white-light corona data

A distinctive feature of the February 25, 2014 CME is that at small distances $R < 1.4R_0$ the explosive expansion of the erupted magnetic flux tube causes the CME FS and the blast shock wave to form. The question arises as to what happens at large distances and whether or not a piston shock wave appears. We can answer it using LASCO C2 and C3 white-light corona data. However, between 00:48:05 and 01:25:50 UT when the CME was in the C2 field, there is no C2 data available.

At 00:48:05 UT, the CME was outside the C2 field, i.e. at $R < 2R_0$, while at 01:25:50 UT the CME leading part was already on the edge of the C2 field, i.e. at $R \approx (6 \div 7)R_0$. We therefore use data from LASCO C3 whose field of view is $\sim (3.7 \div 30)R_0$.

Figure 10 presents white-light corona running difference brightness images for two consecutive times from LASCO C3. The CME frontal structure is clearly seen in them. To resolve the FS leading part and its dynamics, we have plotted running difference brightness distributions $\Delta P_R(R)$ in the direction of the position angle $PA = 115°$ at $\delta\alpha = 2°$.

The results are given in Figure 11. In the distributions $\Delta P_R(R)$ for the CME leading part for three consecutive times (Figure 11, *a–c*) are three characteristic regions corresponding to CME FS (vertical hatching), shock-heated plasma (oblique hatching), and collisional shock wave (light gray background).

Since the front has a foot, then, according to [Eselevich, Eselevich, 2011], in these cases the front width δ_F is defined as the scale on which the brightness jump ΔP_F at the front decreases from the maximum value immediately behind the front to 1/10 of the value (in Figure 11, *c*, the level of $1/10\Delta P_F$ is shown by a horizontal dashed line). With distance away from the Sun, δ_F increases. At $R \approx 15R_0$ (Figure 11, *d*) at the leading edge of the front, a new discontinuity (circled) is formed whose width $\delta_F^* \approx 0.2R_0$ is of the order of the C3 spatial resolution $K_{C3} \approx 0.12R_0$ and practically does not vary with distance (Figure 11, *e–h*).

We try to depict a unified kinematic pattern of this event at distances from $R \approx (1.0 \div 1.4)R_0$ to $R \approx (7 \div 21)R_0$ in the direction of $PA = 112°$–115° at $\alpha = 0°$. To do this, for $R < 1.4R_0$ we use the data presented in Figure 9, but we construct a plot not in the direction of $\alpha = 60°$ but in the direction of $\alpha = 0°$, using the relation $R(r, \alpha = 0°) = r(r, \alpha = 60°) + 1.12R_0$, where $R_c = 1.12R_0$ is the position of the center O. It is quite possible, since the expansion of the arcades that form CME FS relative to the center O occurs in the directions of $\alpha = 0°$ and $\alpha = \pm 60°$ with almost equal velocities. Continuation of this kinematic curve in $R \approx (7 \div 21)R_0$ is constructed from the profiles $\Delta P_R(R)$ in Figure 11, in which for different points in time FS posi-
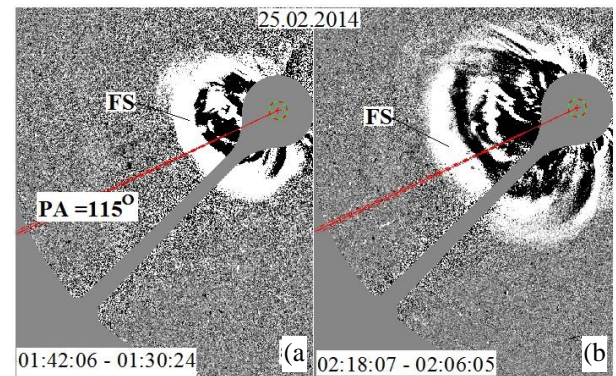

Figure 10. White-light running difference brightness images for two consecutive times according LASCO C3 data. The solid line indicates the direction of $PA = 115°$; dashed lines, $\delta\alpha = 2°$. The February 25, 2014 event

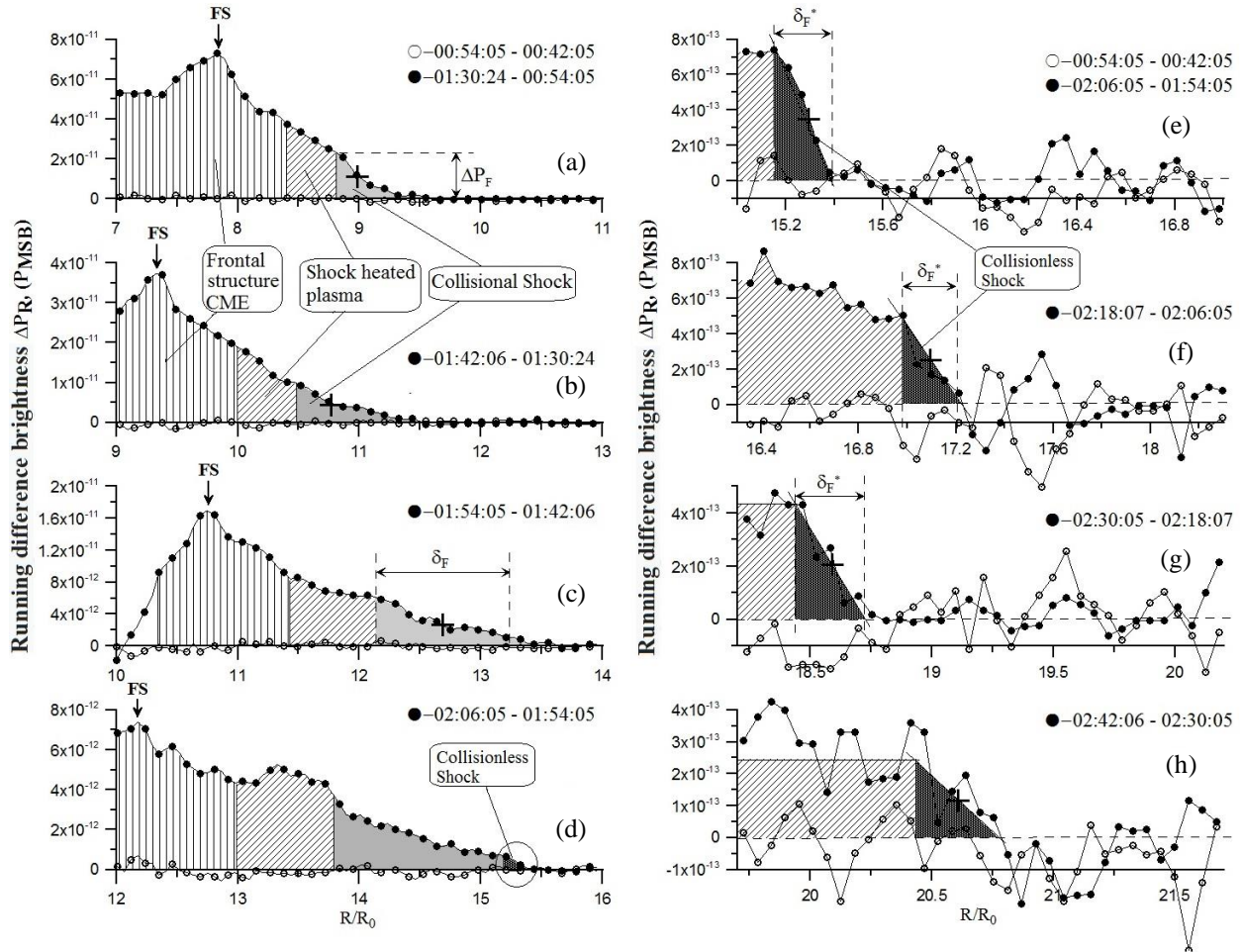*Figure 11.* White-light running difference brightness distributions ΔP_R as a function of R (according LASCO C3 data) for successive points in time in the direction of the position angle $PA=115°$ at $\delta\alpha=2°$ on smaller (*a–d*) and larger (*e–h*) spatial scales. The February 25, 2014 event

tions are indicated by vertical arrows (*a–d*); and positions of the middle point of the shock front, by crosses (*e–h*). Thus constructed kinematic curves of $R(t)$ for FS (black circles), collisional shock (black triangles) and collisionless (crosses) fronts are shown in Figure 12, *a*.

At $R<1.5R_0$ are only points for FS that virtually merge due to small distances between them. The velocities V estimated from the curves of $R(t)$ as a function of R by the above method are shown in Figure 12, *b* for FS (black circles) and blast shock wave (open triangles), as well as at $R>7R_0$ for collisional (black triangles) and collisionless (crosses) shock waves.

The thickened curve shows the Alfvén velocity dependence $V_a(R)$ [Mann et al., 1999, 2003]; the dotted curve indicates slow quasi-stationary solar wind velocities $V_{SW}(R)$ [Wang et al., 2000].

It is not inconceivable that in different active regions the $V_a(R)$ variation may differ from the averaged dependence obtained in [Mann et al., 1999, 2003]. But it is easy to see that such a difference at distances greater than $10\ R_0$ cannot be large. Otherwise, assuming that the plasma density and the radial field component vary with distance at $r>10R_0$ according to the law $\sim 1/R^2$ confirmed by observations, we can show that in Earth's orbit val-

ues of the magnetic field and plasma density used to calculate $V_a(R)$ will differ from observed ones. For this reason, the conclusion is certain that the brightness jumps we observe at $r>10R_0$ in view of the high velocity of their associated structures compared to the slow wind correspond to shock waves. As for the brightness jumps at $r<2R_0$, then, taking into account possible variations in the plasma density and magnetic field strength, at these small distances it is difficult to expect a change in the Alfvén velocity in different active regions to values exceeding those of the velocity V, which, as has been shown, varies in the range from 1250 to 1600 km/s. Therefore, our conclusion that the observed brightness jumps at $r<2R_0$ are driven by shock waves also seems correct.

Thus, from Figure 12, *b* it is evident that the excitation condition for a shock wave before CME $u(R)=V_{FS}(R)-V_{SW}(R)>V_a$ holds at all distances $1R_0<R<20R_0$.

Unlike the distances $R<1.4R_0$ at which the blast shock wave velocity V_{Sh} decreases rapidly with distance, at $R>7R_0$ V_{Sh} first increases and then varies little with distance R (Figure 12, *b*). The distance between FS and the shock front varies little (black triangles and black circles in Figure 12, *a*). This means that the wave
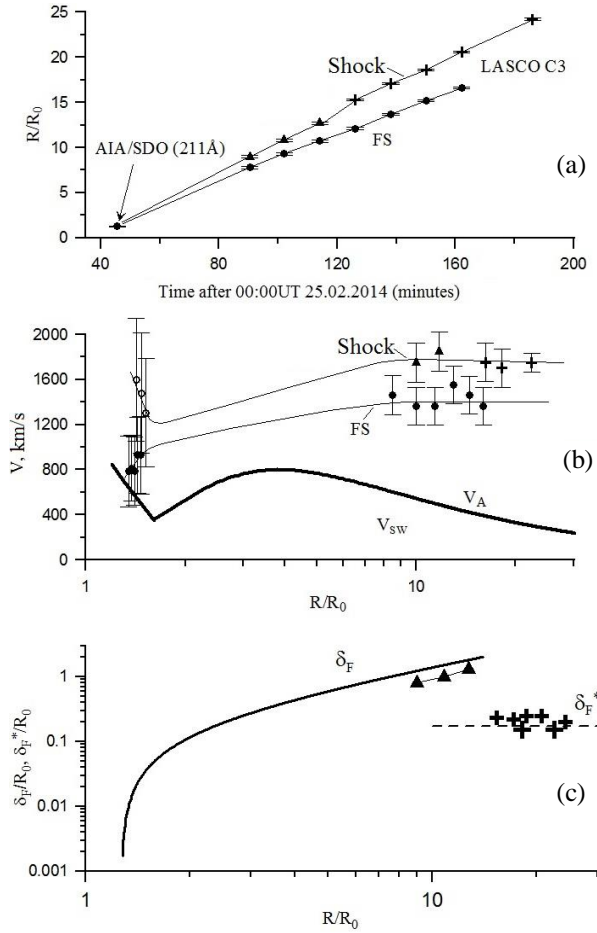
Figure 12. Panel *a* — kinematic dependence $R(t)$ for the frontal structure (FS, black circles) and the shock front (black triangles and crosses) in the direction of $PA=115°$ at $\delta\alpha=2°$. At $R<1.5R_0$, points for the frontal structure are plotted from the 211 Å channel data; at $R>1.5R_0$, from LASCO C3 white-light corona data. Panel *b* — distance R dependences of the CME frontal structure velocity V (black circles), collisional (black triangles) and collisionless shock fronts (black crosses), calculated from the curves on panel *a*. At $R<1.5\,R_0$, velocities of the frontal structure (black circles) and the blast shock wave (open triangles) are from Figure 9, *b* (for more detail, see the text). The solid curve is the estimated Alfvén velocity V_a in the coronal streamer belt from [Mann et al., 1999, 2003], the dotted curve is the velocity V_{SW} of the quasi-stationary slow SW in the streamer belt from [Wang et al., 2000]. Panel *c* — widths of shock fronts of collisional (δ_F, filled triangles) and collisionless (δ_F*, crosses) waves. The solid curve and horizontal dashes show dependences of front widths $\delta_F(R)$ and δ_F* (R) respectively from [Eselevich, Eselevich, 2012], obtained by averaging the data for more than ten CMEs with velocities less than 1500 km/s (according to C3 data). The February 25, 2014 event

energy is replenished from a piston, which is CME. Thus, at $R>7R_0$ the shock wave is "piston". To define the CME-related type of shock wave, we will use the term "piston", implying that in addition to the piston mechanism of shock wave generation determined by continuous expansion of CME boundary (piston), at the super-Alfvén velocity of gradual CME motion relative to the ambient solar wind the mechanism of bow shock wave generation also works.

In Figure 12, *c*, the solid curve shows the dependence of the collisional shock front width $\delta_F(R) \sim \lambda_p$, plotted

in [Eselevich, 2010; Eselevich, Eselevich, 2012] from analysis of more than a dozen CMEs with velocities from several hundreds to $\Sigma \approx 2500$ km/s. In our case, the black triangles are close to this curve. The collisionless shock front width δ_F* (crosses in Figure 12, *c*) is close to the C3 spatial resolution $K_{C3} \approx 0.12R_0$ (horizontal dashes), which also agrees with the conclusions drawn in [Eselevich, Eselevich, 2012].

CONCLUSIONS

Formation of the February 25, 2014 CME is driven by the ejection and subsequent explosive expansion of the magnetic rope whose occurrence, according to [Chen et al., 2014], is due to tether-cutting reconnection.

The resulting full pressure (thermal plus magnetic) impulse affects the overlying coronal arcades, leading to their merging and the formation of a rapidly moving frontal structure of the CME.

This pressure impulse triggers a blast collisional shock wave before the CME whose velocity decreases rapidly with distance.

At large distances $R>7R_0$ before the CME, a "piston" collisional shock wave is detected whose velocity varies little with distance.

At $R \geq 15R_0$, a transition occurs from collisional to collisionless shock wave.

REFERENCES

Alekseenko S.V., Dudnikova G.I., Romanov V.A., Romanov D.V., Romanov K. Magnetic field instabilities in the solar convective zone. *Rus. J. Eng. Thermophys*. 2000, vol. 10, pp. 243–262.

Amari T., Luciani J.F., Mikic Z., Linker J. A twist flux rope model for coronal mass ejections and two-ribbon flare. *Astrophys. J*. 2000, vol. 529, pp. L49–L52. DOI: 10.1086/312444.

Antiochos S.K., DeVore C.R., Klimchuk J.A. A model for solar coronal mass ejections. *Astrophys. J*. 1999, vol. 510, no. 1, pp. 485–493. DOI: 10.1086/306563.

Archontis V., Hood A.W. A flux emergence model for solar eruptions. *Astrophys. J*. 2008, vol. 674, pp. L113–L116. DOI: 10.1086/529377.

Bemporad A., Raymond J., Poletto G., Romoli M. A comprehensive study of the initiation and early evolution of a coronal mass ejection from ultraviolet and white-.light data. *Astrophys. J*. 2007, vol. 655, pp. 576–590. DOI: 10.1086/509569.

Chen H., Zhang J., Cheng X., Ma S., Yang S., Li T. Direct observations of tether-cutting reconnection during a major solar event from 2014 February 24 to 25. *Astrophys. J. Lett*. 2014, vol. 797, no. 2, L15, 7 p. DOI: 10.1088/2041-8205/797/2/L15.

Eselevich M.V. Detecting the width of shock front preceding CME. *Astronomy Report*. 2010, vol. 54, no. 2, pp. 197–208.

Eselevich M.V., Eselevich V.G. Some properties of the development of the perturbed zone and shock preceding a coronal mass ejection. *Astronomy Reports*. 2011, vol. 55, no. 11, pp. 1038–1050.

Eselevich V., Eselevich M. Disturb zone and piston shock ahead of coronal mass ejection. *Astrophys. J*. 2012, vol. 761, no. 1, 10 p. DOI: 10.1088/0004-637X/761/1/68.

Eselevich V.G., Eselevich M.V. The role of rising magnetic tubes in the formation of impulsive coronal mass ejec-

tions. *Astronomy Reports*. 2013, vol. 57, no. 11, pp. 860–871. DOI: 10.1134/S1063772913110012.

Eselevich V.G., Eselevich M.V. Physical differences between the initial phase of the formation of two types of coronal mass ejections. *Reports Astronomy* . 2014, vol. 58, no. 4, pp. 260-271. DOI: 10.1134/S1063772914030032.

Eselevich V.G., Eselevich M.V. Differences in the development of the initial phase of the formation of two types of coronal mass ejections. *Cosmic Res*. 2015, vol. 53, no. 1, pp. 21–30. DOI: 10.1134/S0010952515010049.

Eselevich V.G., Eselevich M.V., Romanov V.A., Romanov D.V., Romanov K.V., Kucherov N.V. Physical mechanisms for the generation of coronal mass ejections from the upper layers of the convective zone. *Izvestiya Krymskoi Astrofizicheskoi Observatorii* [Bulletin of the Crimean Astrophysical Observatory]. 2013, vol. 109, no. 4, pp. 54–60. (In Russian).

Eselevich V.G., Eselevich M.V., Zimovets I.V., Rudenko G.V. Initial formation of an "impulsive" coronal mass ejection. *Astronomy Reports*. 2016, vol. 60, no. 11, pp. 1016–1027. DOI: 10.1134/S1063772916100024.

Fainshtein V.G., Egorov Ya.I. Initiation of CMEs associated with filament eruption, and the nature of CME related shocks. *Adv. Space Res*. 2015, vol. 55, iss. 3, pp. 798–807. DOI: 10.1016/j.asr.2014.05.019.

Gibson E. *Spokoinoe Solntse* [The Quiet Sun]. Moscow, Mir Publ., 1977, pp. 125–146. (In Russian). (English edition: Gibson E.G. The Quiet Sun. National Aeronautics and Space Administration, Scientific and Technical Information Office, 1973, 330 p.).

Gibson S.E., Foster D., Burkepile J., de Toma G., Stanger A. The calm before the storm: The link between quiescent cavities and coronal mass ejections. *Astrophys. J*. 2006, vol. 641, no. 1, pp. 590–605. DOI: 10.1086/500446.

Grechnev V.V., Uralov A.M., Kochanov A.A., Kuzmenko I.V., Prosovetsky D.V., Egorov Y.I., Fainshtein V.G., Kashapova L.K. A tiny eruptive filament as a flux-rope progenitor and driver of a large-scale CME and wave. *Solar Phys*. 2016, vol. 291. pp. 1173–1208. DOI: 10.1007/s11207-016-0888-z.

Grechnev V.V., Lesovoi S.V., Kochanov A.A., Uralov A.M., Altyntsev A.T., Gubin A.V., Zhdanov D.A., Ivanov E.F., Smolkov G.Ya., Kashapova L.K. Multi-instrument view on solar eruptive events observed with the Siberian Radioheliograph: From detection of small jets up to development of a shock wave and CME. *JASTP*. 2018, vol. 174, pp. 46–65. DOI: 10.1016/j.jastp.2018.04.014.

Hundhausen A.J. Coronal mass ejections. *The Many Faces of the Sun: A Summary of the Results from NASA's Solar Maximum Mission*. New York, Springer, 1999, pp. 143–200.

Kliem B., Titov V.S., Török T. Formation of current sheets and sigmoidal structure by the kink instability of a magnetic loop. *Astron. Astrophys*. 2004, vol. 413, no. 3, pp. L23−L26. DOI: 10.1051/0004-6361:20031690.

Krall J., Chen J., Santoro R. Drive mechanisms of erupting solar magnetic flux ropes. *Astrophys. J*. 2000, vol. 539, pp. 964–982. DOI: 10.1086/309256.

Lemen J.R., Title A.M., Akin D.J., Boerner P.F.,·Chou C., Drake J.F., Duncan D.W.,·Edwards C.G.,·Friedlaender F.M., et al. The Atmospheric Imaging Assembly (AIA) on the Solar Dynamics Observatory (SDO). *Solar Phys*. 2012, vol. 275, pp. 17–40. DOI: 10.1007/s11207-011-9776-8.

MacQueen R.M., Fisher R.R. The kinematics of solar inner coronal transients. *Solar Phys*. 1983, vol. 89, pp. 89–102. DOI: 10.1007/BF00211955.

Magara T., Longcope D.W. Sigmoid structure of an emerging flux tube. *Astrophys. J*. 2001, vol. 559, pp. L55–L59. DOI: 10.1086/323635.

Mann G., Aurass H., Klassen A., Estel C., Thompson B.J. Coronal transient waves and coronal shock waves. *ESA SP-446: Plasma Dynamics and Diagnostics in the Solar Transition Region and Corona. Proc. 8th SOHO Workshop (22–25 June 1999, Paris, France)*. 1999, p. 477.

Mann G., Klassen A., Aurass H., Classen H.-T. Formation and development of shock waves in the solar corona and the near-Sun interplanetary space. *Astron. Astrophys*. 2003, vol. 400, pp. 329–336. DOI: 10.1051/0004-6361:20021593.

Moore R.L., LaBonte B.J. The filament eruption in the 3B flare of July 29, 1973: Onset and magnetic field configuration. *Solar and Interplanetary Dynamics. International Astronomical Union / Union Astronomique Internationale (Symposium No. 91 held in Cambridge, Massachusetts, U.S.A. August 27–31, 1979)*. Springer, Dordrecht, 1980, pp. 207–211. DOI: 10.1007/978-94-009-9100-2_32.

Moore R.L., Sterling A.C., Hudson H.S., Lemen J.R. Onset of the magnetic explosion in solar flares and coronal mass ejections. *Astrophys. J*. 2001, vol. 552, no. 2, pp. 833–848. DOI: 10.1086/320559.

Moreno-Insertis F., Schussler M., Ferriz-Mas A. Storage of magnetic flux tubes in a convective overshoot. *Astron. Astrophys*. 1992, vol. 264, no. 2, pp. 686–700.

Patsourakos S., Vourlidas A., Stenborg G. Direct evidence for a fast coronal mass ejection driven by the prior formation and subsequent destabilization of a magnetic flux rope. *Astrophys. J*. 2013, vol. 764, no. 2, 125, 13 p. DOI: 10.1088 / 0004-637X / 764/2/125 .

Priest E.R. *Solnechnaya magnitogidrodinamika* [Solar magnetohydrodynamics]. Moscow, Mir Publ., 1985, p. 89. (In Russian). (English edition: Priest E.R. Solar Magnetohydrodynamics. Springer Netherlands, 1982, 469 p. (Geophysics and Astrophysics Monographs, vol. 21)).

Romanov V.A., Romanov D.V., Romanov K.V. Outburst of magnetic fields from the zone of action of the solar dynamo into the atmosphere of the Sun. *Astronomicheskii zhurnal* [Astronomy Reports]. 1993a, vol. 70, pp. 1237–1246. (In Russian).

Romanov V.A., Romanov D.V., Romanov K.V. The ejection of magnetic fields from the solar dynamo to the relaxation zone. *Astronomicheskii zhurnal* [Astronomy Reports]. 1993b, vol. 70, pp. 1247–1256. (In Russian).

Schmieder B., Démoulin P., Aulanier G. Solar filament eruptions and their physical role in triggering coronal mass ejections. *Adv. Space Res*. 2013, vol. 51, iss. 11, pp. 1967–1980. DOI: 10.1016/j.asr.2012.12.026.

Sheeley N.R.Jr., Walter H., Wang Y.-M., Howard R.A. Continuous tracking of coronal outflows: Two kinds of coronal mass ejections. *J. Geophys. Res*. 1999, vol. 104, no. A11, pp. 24739–24768. DOI: 10.1029/1999JA900308.

Shen Y., Liu Y., Su J. Sympathetic partial and full filament eruptions observed in one solar breakout event. *Astrophys. J*. 2012, vol. 750, 12, 13 p. DOI: 10.1088/0004-637X/750/1/12.

Sterling A.C., Moore R.L. Slow-rise and fast-rise phases of an erupting solar filament, and flare emission onset. *Astrophys. J*. 2005, vol. 630, no. 2, pp. 1148–1159. DOI: 10.1086/432044.

Temmer M., Veronig A.M., Vršnak B., Rybák J., Gömöry P., Stoiser S., Maričić D. Acceleration in fast halo CMEs and synchronized flare HXR bursts. *Astrophys. J. Lett*. 2008, vol. 673, pp. L95–L98. DOI: 10.1086/527414.

Thernisien A., Vourlidas A., Howard R.A. Forward modeling of coronal mass ejection using STEREO/SECCHI data. *Solar Phys*. 2009, vol. 256, pp. 111–130. DOI: 10.1007/s11207-009-9346-5.

Vernazza J.E., Avrett E.H., Loeser R. Structure of the solar chromophere. Basic computations and summary of the results. *Astrophys. J*. 1973, vol. 184, pp. 605–631. DOI: 10.1086/152353.

Vernazza J.E., Avrett E.H., Loeser R. Structure of the solar chromophere. II. The underlying photosphere and tempera-

ture-minimum region. *Astrophys. J. Suppl. Ser.*1976, vol. 30, pp. 1–60. DOI: 10.1086/190356.

Wang Y.-M., Sheeley N.R., Socker D.G., Howard R.A., Rich N.B. The dynamical nature of coronal streamers. *J. Geophys. Res*. 2000, vol. 105, pp. 25,133–25,142. DOI: 10.1029/2000 JA000149.

Zagainova Iu.S., Fainshtein V.G. How do fast impulse CMEs related to powerful flares but unrelated to eruptive filaments appear and move? *Adv. Space Res*. 2015, vol. 55, iss. 3, pp. 822–834. DOI: 10.1016/j.asr.2014.05.032.

Zhang J., Wang J., Deng Y., Wu D. Magnetic flux cancellation associated with the major solar event on 2000 July 14. *Astrophys. J*. 2001, vol. 548, pp. L99–L102.

URL: https://www.nso.edu/telescopes/nisp (accessed March 27, 2020).

URL: http://gong2.nso.edu (accessed March 27, 2020).